This is the accepted manuscript made available via CHORUS. The article has been published as:

Magnetic phase transition, magnetoresistance, and anomalous Hall effect in Ga-substituted math xmlns="http://www.w3.org/1998/Math/MathML">mrow>mi mathvariant="normal">Y/mi>msub>mi>Mn/mi>mn>6/mn >/msub>msub>mi>Sn/mi>mn>6/mn>/msub>/mrow>/ma th> with a ferromagnetic kagome lattice

C. Q. Xu, T. W. Heitmann, H. Zhang, Xiaofeng Xu, and X. Ke

Phys. Rev. B **104**, 024413 — Published 9 July 2021

DOI: 10.1103/PhysRevB.104.024413

Magnetic Phase Transition, Magnetoresistance, and Anomalous Hall Effect in Ga-substituted YMn_6Sn_6 with Ferromagnetic Kagome Lattice

C. Q. Xu[1,2], T. W. Heitmann[3], H. Zhang[1], Xiaofeng Xu[2], X. Ke[1]

[1] *Department of Physics and Astronomy, Michigan State University, East Lansing, Michigan 48824-2320, USA*

[2] *Department of Applied Physics, Zhejiang University of Technology, Hangzhou 310023, China*

[3]*Missouri Research Reactor and Department of Physics and Astronomy, University of Missouri, Columbia, Missouri 65211, USA*

The $HfFe_6Ge_6$-type RMn_6Sn_6, a metallic system consisting of ferromagnetic Kagome planes of Mn, has been recently shown to be a candidate hosting topological electronic properties. In this paper, we report magnetic and electronic properties in $YMn_6Sn_{6-x}Ga_x$ single crystals via magnetic susceptibility, electrical transport, and single crystal neutron diffraction measurements. We show that the magnetic ground state of $YMn_6Sn_{6-x}Ga_x$ ($0 \leq x \leq 0.61$) evolves from incommensurate antiferromagnet to ferromagnet with increasing Ga substitution x, a feature which is accompanied by the decrease in magnetoresistance. Furthermore, the topological Hall effect observed in the pristine compound is absent in the Ga-substituted ones; instead, the anomalous Hall effect persists which may be associated with the Berry curvature of gapped Dirac bands near the Fermi energy. These results suggest strong correlation between electronic properties and magnetism in this topological magnet that can be readily tuned via Ga substitution.

After the experimental discovery of the topological insulators[1,2], research on topological electronic materials has been a subject of flourishing interest in the past nearly two decades. In particular, by integrating magnetism with nontrivial electronic band topology, a variety of novel quantum phenomena has been predicted and/or observed more recently[3], such as quantum anomalous Hall effect[4], Chiral anomaly[5], Axion insulator state[6,7], etc. Thus, researchers in both condensed matter physics and materials science communities have been continuously exploring new magnetic topological materials[8]. Among these, metallic systems with magnetic Kagome lattice, such as Fe_3Sn_2 [9,10], FeSn [11], and $Co_3Sn_2S_2$ [12-15], have been attracting increasing attention recently. On the one hand, with magnetic ions occupying the Kagome lattice, potential magnetic frustration associated with the Kagome lattice structure may give rise to complex magnetism, which can in turn affect the electronic band structures. On the other hand, the geometric frustration of Kagome lattice leads to destructive interferences, i.e, phase cancellation of Bloch wave functions, leading to flat bands (i.e., macroscopically degenerate manifold of single-particle states) and fractional quantum Hall effect via appropriate band filling[16,17]. Furthermore, the intrinsic spin-orbit coupling associated with the magnetic Kagome lattice gives rise to artificial magnetic flux and opens the bandgap on the Dirac points, resulting in nontrivial electronic bands with non-zero Chern number[18,19].

More recently, the RMn_6Sn_6 (R = rare earth, Y, Sc, and Lu) family of materials have emerged as a new platform to investigate the topological electronic properties. RMn_6Sn_6 crystallizes in the P6/mmm (No. 191) space group, where a unit cell contains two layers of Mn atoms, each of which forms a Kagome web in the ab plane. For instance, it was discovered that $TbMn_6Sn_6$ shows distinct Landau quantization of electronic states in the presence of magnetic field and the quantized Landau fan structure features spin polarized Dirac dispersion with a large Chern

gap[20]. Importantly, it has been shown via scanning tunneling microscopy/spectroscopy(STM/STS) that the Landau quantization is only observed on the Mn Kagome plane terminated surface but not on the TbSn terminated surface, providing appealing evidence that Mn Kagome plane indeed dominates the nontrivial topological electronic properties[20]. Anomalous Hall effect has also been observed in RMn_6Sn_6 with paramagnetic rare-earth ions R [21,22], while topological Hall effect has been observed in YMn_6Sn_6 which is attributed to a field-induced double fan spin structure [23] or a transverse conical spiral structure[24]. On the other hand, the magnetism of $RMn_6(Sn,Ge)_6$ was initially investigated more than two decades ago, and it was found that the spin structure of this system strongly depends on R ions. For compounds with nonmagnetic R ions (R = Y, Sc, and Lu), the antiferromagnetic spin structure is described as a staggered spiral or "double flat spiral" along the *c*-axis while spins within each Kagome remain ferromagnetically aligned in the *ab* plane[25,26]. In contrast, for compounds with paramagnetic R ions, the system exhibits ferrimagnetic ground state with spins of all Mn Kagome planes aligned parallel and spins of R ions aligned antiparallel to Mn spins[27]. These distinct magnetic structures in RMn_6Sn_6 arise from the competition of magnetic exchange interactions between various neighbors along the c-axis and the R-Mn antiferromagnetic coupling for compounds with paramagnetic R. It is also found that these competing magnetic exchange interactions in compounds with nonmagnetic R ions can be readily tuned by partially replacing (Ge,Sn) with Ga or replacing R with divalent alkaline earth metal ions such that antiferro-magnetism in the pristine compounds is turned into ferromagnetism in the substituted compounds[28-30]. An interesting question naturally arises: how does the change of the magnetism affect the electronic properties in the substituted compounds, considering that magnetism and electronic properties in this system are intimately intertwined?

In this work, we report both magnetic and electronic transport properties of $YMn_6Sn_{6-x}Ga_x$ via magnetic susceptibility, single crystal neutron diffraction, magnetotransport and Hall effect measurements. We show that the system undergoes magnetic phase transitions from incommensurate to the coexistence of commensurate and incommensurate and eventually to ferromagnetic with increasing Ga concentration x. Concurrently, the magnitude of magnetoresistance decreases with the increase of x and nearly saturates when the ferromagnetic phase dominates. In addition, the topological Hall effect observed in the pristine compound evolves into anomalous Hall effect associated with the ferromagnetic phase for compounds with larger x.

Single crystals $YMn_6Sn_{6-x}Ga_x$ ($0 \leq x \leq 0.61$) were fabricated via Sn flux methods[31]. High purity yttrium pieces, manganese pieces, tin shots, and gallium ingots were mixed with the molar ratio of $1 : 6 : 30 : x_N$ as the starting material, x_N is nominal value. The actual Ga concentration x is determined using an energy-dispersive x-ray spectroscopy (EDX) and its relationship with x_N is shown in Fig. S1 in the Supplemental Materials[32]. Magnetic susceptibility measurements of $YMn_6Sn_{6-x}Ga_x$ were conducted using a Superconducting Quantum Interference Device (SQUID), and electronic transport measurements were performed using a Physical Property Measurement System (PPMS), both from Quantum Design. Single crystal neutron diffraction measurements were carried out on a triple-axis spectrometer (TRIAX) with incident neutron wavelength of 2.359Å (14.7meV) at the University of Missouri Research Reactor. Two different collimator settings of 60'-60'-S-40'-40' and 60'-20'-S-20'-20' were used in this experiment and single crystal samples were measured in the (H 0 L) scattering plane, where H and L are in reciprocal lattice units (*r. l. u.*).

Figure 1(a) shows the temperature dependence of magnetization $M(T)$ for various doping level x measured in the presence of 0.1 T magnetic field applied along the [1 0 0] direction. The samples were initially zero-field cooled (ZFC), although we found that there is no difference between ZFC and FC measurements. An expanded view of the high temperature region for samples with small x is depicted in Fig. 1(b). One can clearly see that the $M(T)$ behavior of $YMn_6Sn_{6-x}Ga_x$ significantly depends on x. For $x \leq 0.04$, the magnitude of M is much smaller and there are two kinks in the $M(T)$ data, indicating two magnetic phase transitions; for $x = 0.07$, only one peak in $M(T)$ is observed; for $x = 0.13, 0.22, \text{and } 0.30$, M sharply increases at high temperature and then decreases at lower temperature, while for $x = 0.61$ M saturates at low temperature. These distinct features highlight complex x dependent magnetic phase transitions. A similar trend of the evolution of $M(T)$ with x has been observed in polycrystalline $YMn_6Sn_{6-x}Ga_x$ compounds[33]. Figure 1(c) presents the isothermal magnetization $M(B)$ measurements of $YMn_6Sn_{6-x}Ga_x$ at $T = 10$ K. For small doping level x, spin-flop transition is clearly observed, indicating an antiferromagnetic ground state at zero field. With increasing x, the critical field of the spin-flop transition decreases and the transition nearly vanishes for $x > 0.22$; instead, the magnetization rapidly increases and saturates in the presence of small magnetic field. By comparing both $M(T)$ and $M(B)$ data measured with the magnetic field applied along the [100] and [001] (data not shown) directions, we conclude that all $YMn_6Sn_{6-x}Ga_x$ samples studied exhibit an easy-plane magnetic anisotropy. Figure 1(d) shows the x dependence of lattice parameters a and c determined via single crystal neutron diffraction measurements at room temperature, where one can see that both a and c decrease below $x = 0.30$ while they nearly saturate above $x = 0.30$.

Next, we present the variation of magnetic structures induced by Ga substitutions in $YMn_6Sn_{6-x}Ga_x$. Figures 2(a-d) show the false-color T – (0 0 L) contour maps measured at zero

field, i.e., the temperature dependence of neutron scattering intensity of (0 0 L) scans, of $YMn_6Sn_{6-x}Ga_x$ with $x = 0.0, 0.13, 0.22, \text{and } 0.30$. A coarse collimator setting of 60'-60'-S-40'-40' was used. As presented in Fig.2(a), the pristine compound undergoes paramagnetic-to-commensurate (CM) antiferromagnetic phase transition with (0 0 0.5) propagation wave vector at $T_N \sim 350$ K, followed by commensurate-to-incommensurate (ICM) phase transition at $T_{IC} \sim 331$ K [34]. There are two propagation wave vectors (0 0 δ_1) and (0 0 δ_2) associated with the incommensurate phase, as seen in Fig. 3(a) which were measured using a tighter collimator setting of 60'-20'-S-20'-20'. The associated spin structure consists of staggered spiral or "double flat spiral" feature along the c-axis[25,26]. The incommensurability δ_1 and δ_2 are nearly equal to each other ($\delta_1 = 0.358$, $\delta_2 = 0.408$), and both δ_1 and δ_2 decrease at lower temperature while the difference between δ_1 and δ_2 decreases, consistent with previous reports[24,25]. For $x = 0.13$, in contrast to the pristine compound, no commensurate phase is observed before the sample displays an ICM antiferromagnetic phase transition at $T_{IC} \sim 317$ K, as plotted in Fig. 2(b). Two incommensurate peaks at (0 0 $\delta_{1,2}$) are observed as well (Fig. 3(b)), while the values of δ_1 and δ_2 are about 0.086 and 0.149 which are smaller than the incommensurability observed in the parent compound. For $x = 0.22 \text{ and } 0.30$, both T_{IC} and the incommensurability further decrease, as shown in Fig. 2(c,d). Note that two ICM peaks are still visible for both these two compounds, as shown depicted in Fig. 3(c,d). Interestingly, above T_{IC} these two compounds ($x = 0.22 \text{ and } 0.30$) undergo paramagnetic-to-ferromagnetic phase transition at higher temperature and below T_{IC} the ICM phase coexists with the ferromagnetic phase. The existence of a ferromagnetic phase is evidenced by the temperature dependence of the integrated intensity of (0 0 2) Bragg peak plotted in Fig. 2(e,f), which reflects the scattering signal contribution from both ferromagnetism and nuclear scattering. It is worth noting that the ICM component is drastically reduced for the $x = 0.30$ sample, as indicated by the

large reduction in the ICM Bragg peak intensity as well as the large enhancement in magnetic moment shown in Fig. 1(a). With $x = 0.61$, the ICM phase disappears and only the ferromagnetic phase exists below 365 K, as suggested by the monotonic increase in the integrated intensity of (0 0 2) Bragg peak plotted in Fig. 2(f). Figure 4(a) illustrates the complex phase diagram of $YMn_6Sn_{6-x}Ga_x$ determined from both neutron diffraction and magnetic susceptibility measurements, with both commensurate antiferromagnetic phase and the simplified ICM phase shown in Fig. 4(b) and 4(c) respectively.

The decrease of incommensurability and the emergence of ferromagnetic phase in the Ga-substituted $YMn_6Sn_{6-x}Ga_x$ suggest a variation of the competing exchange interactions between neighboring Mn ions along the *c*-axis, while the intraplane exchange interaction remains dominant and ferromagnetic. Along the *c*-axis, two nearest-neighbor exchange interactions of Mn-Sn-Sn-Sn-Mn (J_1) and of Mn-(Y,Sn)-Mn (J_2) are ferromagnetic, while the next-nearest-neighbor exchange interaction (J_3) is negative[26,28]. There are two mechanisms that may account for the change in magnetism in $YMn_6Sn_{6-x}Ga_x$. First, the determined *c*-lattice parameter is found to monotonically decease with increasing Ga substitution in $YMn_6Sn_{6-x}Ga_x$, as shown in Fig. 1(d), which is expected to change the exchange interactions between neighboring Kagome planes and the resultant competition. Second, the Ga-substitution hole-dopes the system, which may lead to an enhancement of density of states near the Fermi level that have contribution from the dispersion along the *c*-axis. This can strengthen the ferromagnetic exchange interactions J_1 and J_2 while weakening the antiferromagnetic one J_3. Previous studies on both $YMn_6Ge_{6-x}Ga_x$ and $LuMn_6Ge_{6-x}Ga_x$ [28,29], in which Ga substitution gives rise to an *expansion* (in contrast to a contraction seen in $YMn_6Sn_{6-x}Ga_x$ studied in this work) along the *c*-axis, also report ferromagnetism induced by partially replacing Ge with Ga. This suggests that the second scenario is more likely the underlying

mechanism for the evolution of magnetic structures upon Ga substitution, which warrants electronic structure calculations on these Ga-substituted compounds in the future.

Now, we discuss the response of electronic transport properties to the change of magnetic structure in $YMn_6Sn_{6-x}Ga_x$. Figure 5(a-f) present the magnetoresistance of several $YMn_6Sn_{6-x}Ga_x$ compounds, which is defined $MR = \frac{\Delta\rho}{\rho_0} \times 100\% = \frac{\rho(B)-\rho(0)}{\rho(0)} \times 100\%$, measured at selected temperatures with the magnetic field applied along the in-plane direction (B // [1 0 0]) and with the current applied along the out-of-plane axis (I // [0 0 1]). One can clearly see that both the shape and the magnitude of MR curves strongly depend on the Ga substitution level x. For the pristine sample and the $x = 0.07$ and $x = 0.13$ samples, there are two field-induced transitions observed in MR curves which are associated with the spin-flop transition and the saturation of magnetic momentum respectively, consistent with the isothermal magnetization measurements $M(B)$ shown in Fig. 1(c). Note that upon the spin-flop transition, a double-fan spin structure with c-axis spin component (or a transverse conical spiral structure) is formed as revealed by previous neutron diffraction measurements [23,24]. These transition fields decrease at higher temperature. For compounds with larger x, such field-induced transitions are barely observable, again in agreement with the $M(B)$ shown in Fig. 1(c). Interestingly, as shown in Fig. 5(g) and (h), the magnitude of MR (at large magnetic field when the magnetic momentum approaches being saturated) decreases with increasing x. Such variation of MR is mainly dominated by spin scattering. As determined from the neutron diffraction measurements discussed above, for the pristine compound, in the absence of magnetic field its incommensurate magnetic structure is characterized by two propagation vectors of (0 0 $\delta_{1,2}$) with $\delta_1 \approx \delta_2 \approx 0.266$ at low temperature, which corresponds to a spin rotation angle $\theta \approx 95.6^\circ$ between the spins of neighboring Kagome bilayers (including Mn-Sn-Sn-Sn-Mn) along the c-axis [34]. Therefore, with I // [0 0 1] spin scattering is large at low field

and reduces with increasing field when spins are gradually polarized along the magnetic field direction, leading to large negative MR. By partially substituting Ga for Sn, the incommensurability δ decreases and correspondingly θ decreases. As a result, spin scattering at zero field reduces, and consequently the magnitude of MR monotonically decreases with increasing x. Notably, compared to the pristine compound, *MR* drastically decreases for compounds with larger *x* in which the ferromagnetic phase dominates. *MR* measurements were previously reported on polycrystalline $YMn_6Sn_{6-x}Ga_x$ with $x = 0$, 0.1, and 0.2 at $T = 5$ K, and a *MR* value of ~ 30% at 5 T was observed for the $x = 0.2$ sample [33]. Since $YMn_6Sn_{6-x}Ga_x$ exhibits strong anisotropy in both magnetization and *MR* as shown in Fig. S3 and Fig. S4 in the Supplemental Materials, our current *MR* measurements on single crystals with multiple *x* values measured up to 9 T at various temperatures provide insightful information on the relationship between the observed *MR* features and the magnetic structures.

As mentioned in the introduction, pristine YMn_6Sn_6 exhibits unusual topological Hall effect (with a maximum around 240 K), which was attributed to the field-induced double fan spin structure[23] or a transverse conical spiral structure[24]. Considering the different magnetic structures induced via Ga substitution, this motivates us to investigate the Hall effect of the Ga-substituted compounds. Figure 6(a) shows the Hall resistivity $\rho_{yz}(B)$ measured at $T = 240$ K with the magnetic field applied along the [100] direction for various Ga-doped compounds (including the pristine one for comparison). It is clear that ρ_{yz} exhibits nonlinear field dependence for all samples, characteristic of anomalous contribution to the Hall effect in addition to the ordinary term. Note that we applied $\rho_{yz} = (\rho_{yz}(+B) - \rho_{yz}(-B))/2$ to avoid the longitudinal signal due to potential misalignment of voltage leads. At a first glance, ρ_{yz} of the pristine compound behaves quite differently from other Ga-substituted ones. ρ_{yz} of the pristine compound shows a "S" shape

feature, which is similar to a recent study by Wang et al. [23], while ρ_{yz} of the Ga-substituted ones sharply increases at low field and then nearly saturates at higher field. After subtracting the ordinary Hall effect component, the anomalous Hall resistivity ρ_{yz}^{A} curves are shown in Fig. 6(b). Here ρ_{yz}^{A} consists of conventional anomalous Hall effect and topological Hall effect, the former of which is proportional to magnetization (M) and has contribution from both extrinsic scattering (skew scattering and side-jump) and intrinsic (Berry curvature) mechanisms. By comparing $\rho_{yz}^{A}(B)$ and $M(B)$ shown in Fig. 1(c), we can see that for the Ga-substituted compounds $\rho_{yz}^{A}(B)$ is mainly dominated by the conventional anomalous Hall effect, which is in contrast to the pristine compound wherein topological Hall effect has a significant contribution to $\rho_{yz}^{A}(B)$.

The observation of anomalous Hall effect in $YMn_6Sn_{6-x}Ga_x$ with larger x is interesting, even though it is challenging to separate the intrinsic anomalous Hall effect induced by the Berry curvature from the extrinsic mechanisms. Spins of all Mn Kagome planes in these compounds are parallel aligned, which is reminiscent of the case in $TbMn_6Sn_6$. Distinct from $TbMn_6Sn_6$ whose magnetic moment is perpendicular to the Kagome plane[27], in $YMn_6Sn_{6-x}Ga_x$ the magnetic moment remains in the Kagome plane. Nevertheless, recent ARPES measurements in pristine YMn_6Sn_6 reveal the existence of Dirac points near the Fermi energy with spin polarized bands, which carry intrinsic Berry curvatures[35]. Thus, it is desirable to calculate the intrinsic anomalous Hall effect contributed from the Berry curvature, particularly on $YMn_6Sn_{6-x}Ga_x$ with larger x, and compare it to the ferrimagnetic $TbMn_6Sn_6$ [20]. Furthermore, it would be interesting to investigate the magnetic excitations of ferromagnetic $YMn_6Sn_{6-x}Ga_x$ and compare their spin dynamics to the antiferromagnetic pristine compound which exhibits features of topological magnons[34].

In summary, we have reported magnetic susceptibility, electronic transport, and single crystal neutron diffraction measurements on a series of Ga-substituted $YMn_6Sn_{6-x}Ga_x$. We show that Ga-substituted $YMn_6Sn_{6-x}Ga_x$ undergoes magnetic phase transition from incommensurate antiferromagnetic to ferromagnetic, which is accompanied by the decrease of magnetoresistance. In addition, anomalous Hall effect is observed in all $YMn_6Sn_{6-x}Ga_x$, which is presumably associated with the intrinsic Berry curvature of Dirac bands with Chern gaps that warrants future theoretical investigations. This study suggests strong correlation between electronic properties and magnetism in YMn_6Sn_6 that can be readily tuned via Ga substitution.

Acknowledgements

H.Z. and X.K. thank the financial support by the U.S. Department of Energy, Office of Science, Office of Basic Energy Sciences, Materials Sciences and Engineering Division under Award # DE-SC0019259. Work by C.X. was partially supported by the Start-up funds at Michigan State University.

Figure Captions:

Figure 1. (a) Temperature dependence of magnetization of $YMn_6Sn_{6-x}Ga_x$ with various Ga substitution level x measured with B = 0.1 T. (b) An expanded view of magnetization at high temperature region for compounds with smaller x. (c) Isothermal magnetization curves $M(B)$ measured at T = 10 K. (d) The Ga substitution level x dependence of lattice parameters a and c.

Figure 2. (a-d) T- (0 0 L) false-color contour map of $YMn_6Sn_{6-x}Ga_x$ single crystals with x = 0, 0.13, 0.22, 0.30, respectively. The measurements were conducted using a coarse collimator setting of 60'-60'-S-40'-40'. Note that the data for x = 0 is taken from Ref [34]. Temperature dependence of the integrated neutron scattering intensity of the (0 0 2) magnetic Bragg peak for compounds with x = 0.22 (e) and x = 0.30 and x = 0.61 (f).

Figure 3. (0 0 L) scans of $YMn_6Sn_{6-x}Ga_x$ single crystals with x = 0, 0.13, 0.22, 0.30 measured using a fine collimator setting of 60'-20'-S-20'-20' at selected temperatures. Green and blue dashed curves are two Gaussian fits to the incommensurate peaks with the same full-width-half-maximum. Note that the incommensurability δ is referred to as the position of incommensurate peaks relative to (0 0 1) nuclear Bragg peak in Figure (a) and (0 0 2) nuclear Bragg peak in Figures (b-d).

Figure 4. (a) $T - x$ phase diagram of $YMn_6Sn_{6-x}Ga_x$, extracted from magnetic susceptibility and single crystal neutron diffraction measurements. (b) and (c) present commensurate (CM) and incommensurate (ICM) spin structure, respectively. The ICM spin structure is simplified by neglecting the small spin rotation angle between two neighboring Mn Kagome planes of Mn-Sn-Sn-Sn-Mn [34].

Figure 5. (a-e) Magnetoresistance ($MR = \frac{\Delta\rho}{\rho_0} \times 100\%$) of $YMn_6Sn_{6-x}Ga_x$ single crystals with x = 0, 0.07, 0.13, 0.22, 0.30, and 0.61 measured at various temperatures, respectively. The current is applied along the [0 0 1] direction and magnetic field is applied along the [1 0 0] direction. The x dependence of MR value extracted at 9 T at T = 40 K (e) and 240 K (f). Note that at 40 K the magnetic moment of the pristine compound is not nearly saturated yet. And some compounds with the same x were measured as shown in Figure S2.

Figure 6. (a) Hall resistivity of $YMn_6Sn_{6-x}Ga_x$ single crystals with x = 0, 0.07, 0.13, 0.22, 0.30, and 0.61 measured at T = 240 K. (b) Anomalous Hall resistivity of $YMn_6Sn_{6-x}Ga_x$ after subtracting the ordinary Hall contribution.

Figure 1.

C. Xu et al,

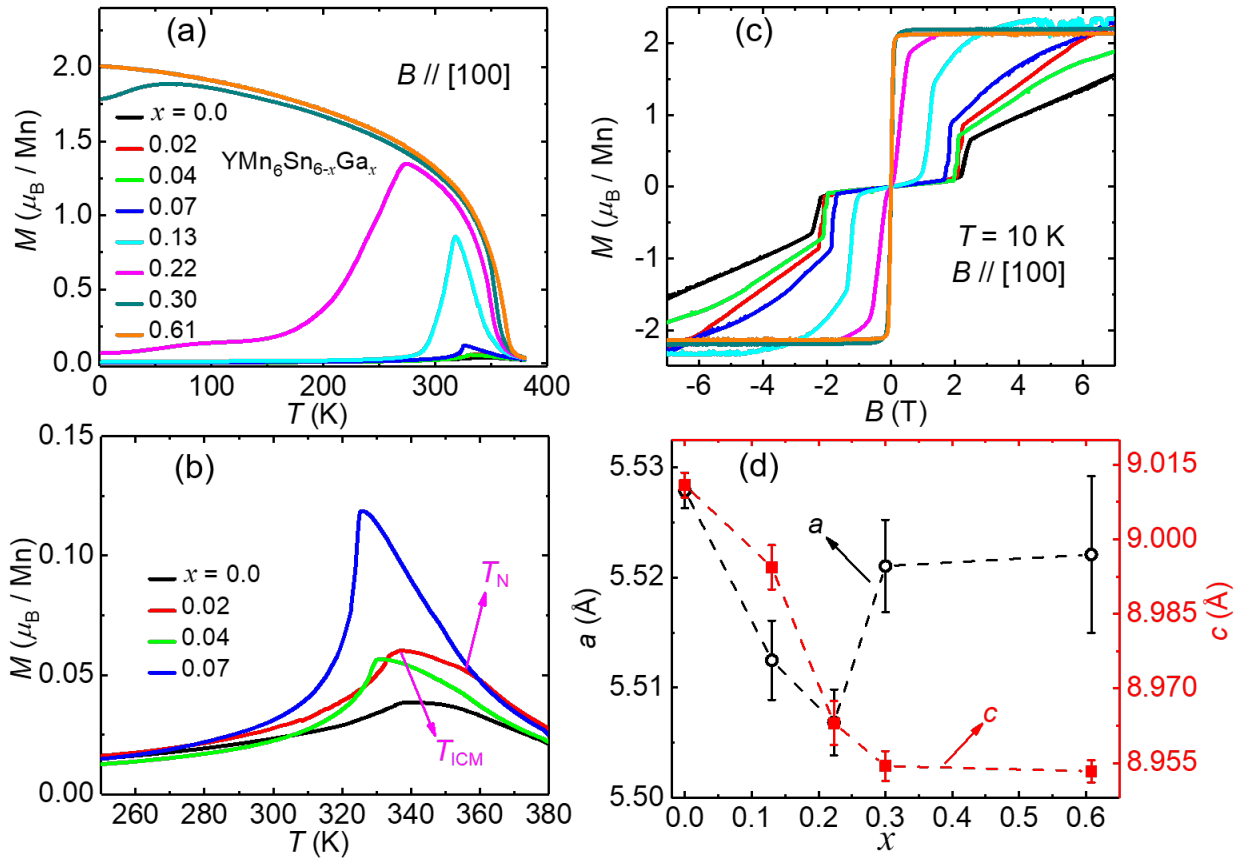

Figure 2.

C. Xu et al,

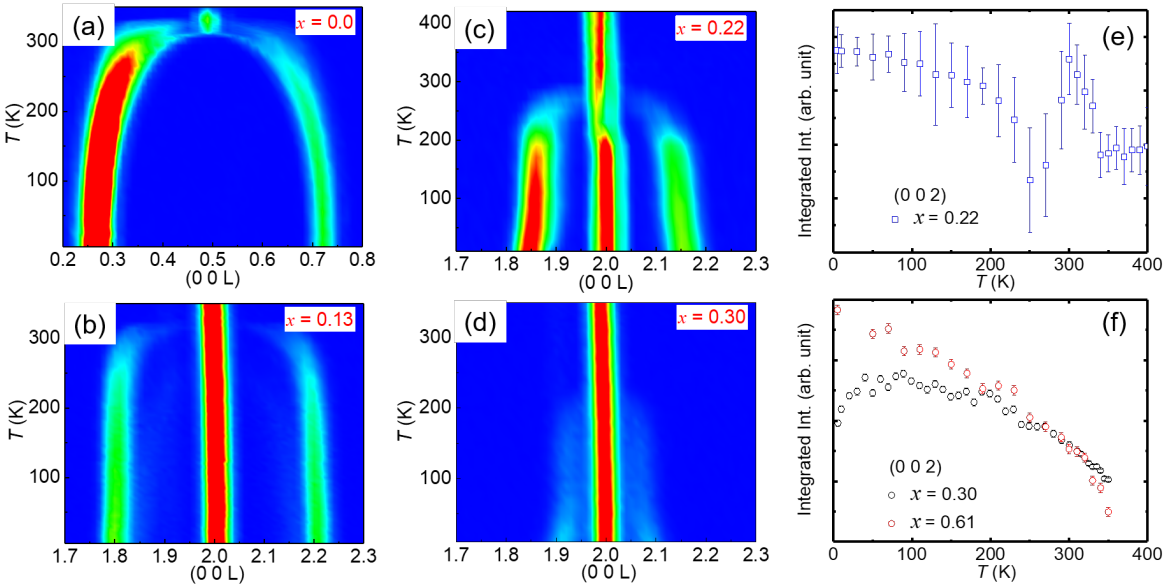

Figure 3.

C. Xu et al,

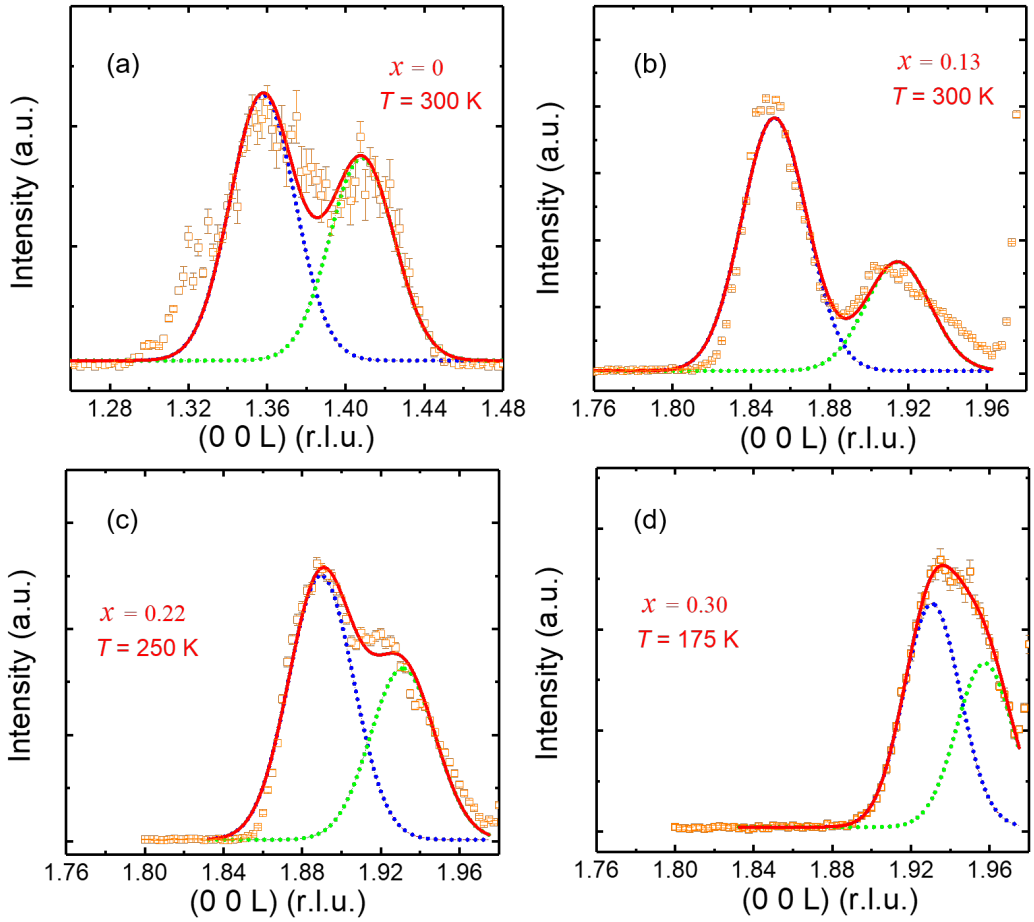

Figure 4.

C. Xu et al,

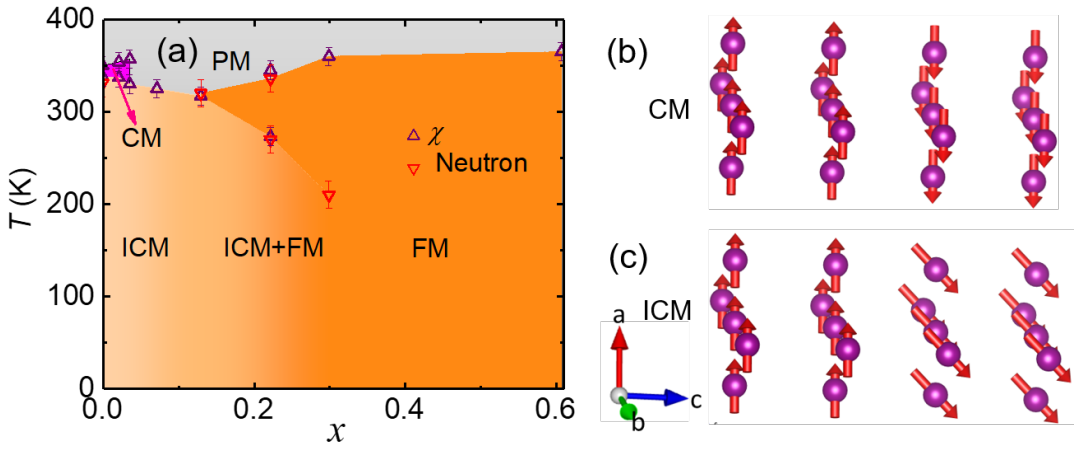

Figure 5.

C. Xu et al,

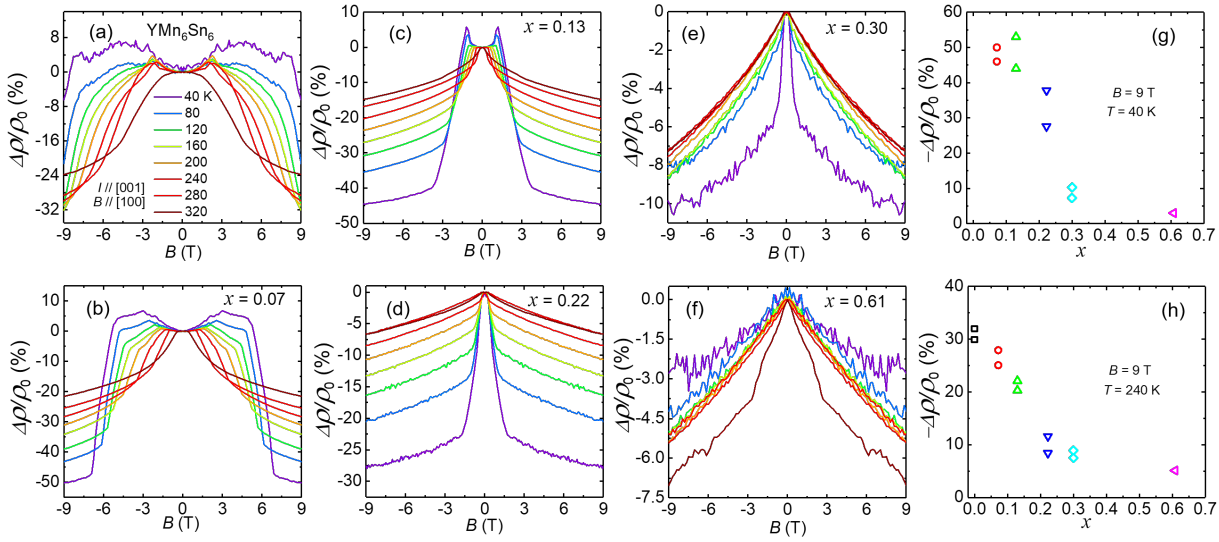

Figure 6.

C. Xu et al,

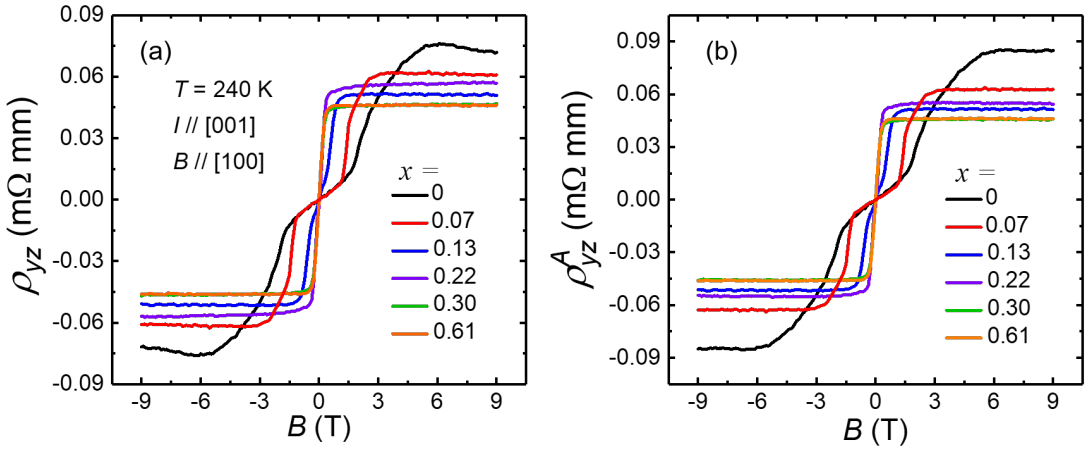

1 Hsieh, D., Qian, D., Wray, L., Xia, Y., Hor, Y. S., Cava, R. J. & Hasan, M. Z. A topological Dirac insulator in a quantum spin Hall phase. *Nature* **452**, 970-974, doi:10.1038/nature06843 (2008).
2 König, M., Wiedmann, S., Brüne, C., Roth, A., Buhmann, H., Molenkamp, L. W., Qi, X.-L. & Zhang, S.-C. Quantum Spin Hall Insulator State in HgTe Quantum Wells. *Science* **318**, 766-770, doi:10.1126/science.1148047 (2007).
3 Tokura, Y., Yasuda, K. & Tsukazaki, A. Magnetic topological insulators. *Nature Reviews Physics* **1**, 126-143, doi:10.1038/s42254-018-0011-5 (2019).
4 Yu, R., Zhang, W., Zhang, H.-J., Zhang, S.-C., Dai, X. & Fang, Z. Quantized Anomalous Hall Effect in Magnetic Topological Insulators. *Science* **329**, 61-64, doi:10.1126/science.1187485 (2010).
5 Jia, S., Xu, S.-Y. & Hasan, M. Z. Weyl semimetals, Fermi arcs and chiral anomalies. *Nature Materials* **15**, 1140-1144, doi:10.1038/nmat4787 (2016).
6 Li, R., Wang, J., Qi, X.-L. & Zhang, S.-C. Dynamical axion field in topological magnetic insulators. *Nature Physics* **6**, 284-288, doi:10.1038/nphys1534 (2010).
7 Mong, R. S. K., Essin, A. M. & Moore, J. E. Antiferromagnetic topological insulators. *Physical Review B* **81**, 245209, doi:10.1103/PhysRevB.81.245209 (2010).
8 Xu, Y., Elcoro, L., Song, Z.-D., Wieder, B. J., Vergniory, M. G., Regnault, N., Chen, Y., Felser, C. & Bernevig, B. A. High-throughput calculations of magnetic topological materials. *Nature* **586**, 702-707, doi:10.1038/s41586-020-2837-0 (2020).
9 Ye, L., Kang, M., Liu, J., von Cube, F., Wicker, C. R., Suzuki, T., Jozwiak, C., Bostwick, A., Rotenberg, E., Bell, D. C., Fu, L., Comin, R. & Checkelsky, J. G. Massive Dirac fermions in a ferromagnetic kagome metal. *Nature* **555**, 638-642, doi:10.1038/nature25987 (2018).
10 Lin, Z., Choi, J.-H., Zhang, Q., Qin, W., Yi, S., Wang, P., Li, L., Wang, Y., Zhang, H., Sun, Z., Wei, L., Zhang, S., Guo, T., Lu, Q., Cho, J.-H., Zeng, C. & Zhang, Z. Flatbands and Emergent Ferromagnetic Ordering in Fe_3Sn_2 Kagome Lattices. *Physical Review Letters* **121**, 096401, doi:10.1103/PhysRevLett.121.096401 (2018).
11 Kang, M., Ye, L., Fang, S., You, J.-S., Levitan, A., Han, M., Facio, J. I., Jozwiak, C., Bostwick, A., Rotenberg, E., Chan, M. K., McDonald, R. D., Graf, D., Kaznatcheev, K., Vescovo, E., Bell, D. C., Kaxiras, E., van den Brink, J., Richter, M., Prasad Ghimire, M., Checkelsky, J. G. & Comin, R. Dirac fermions and flat bands in the ideal kagome metal FeSn. *Nature Materials* **19**, 163-169, doi:10.1038/s41563-019-0531-0 (2020).
12 Liu, E., Sun, Y., Kumar, N., Muechler, L., Sun, A., Jiao, L., Yang, S.-Y., Liu, D., Liang, A., Xu, Q., Kroder, J., Süß, V., Borrmann, H., Shekhar, C., Wang, Z., Xi, C., Wang, W., Schnelle, W., Wirth, S., Chen, Y., Goennenwein, S. T. B. & Felser, C. Giant anomalous Hall effect in a ferromagnetic kagome-lattice semimetal. *Nature Physics* **14**, 1125-1131, doi:10.1038/s41567-018-0234-5 (2018).
13 Morali, N., Batabyal, R., Nag, P. K., Liu, E., Xu, Q., Sun, Y., Yan, B., Felser, C., Avraham, N. & Beidenkopf, H. Fermi-arc diversity on surface terminations of the magnetic Weyl semimetal $Co_3Sn_2S_2$. *Science* **365**, 1286-1291, doi:10.1126/science.aav2334 (2019).
14 Liu, D. F., Liang, A. J., Liu, E. K., Xu, Q. N., Li, Y. W., Chen, C., Pei, D., Shi, W. J., Mo, S. K., Dudin, P., Kim, T., Cacho, C., Li, G., Sun, Y., Yang, L. X., Liu, Z. K., Parkin, S. S. P., Felser, C. & Chen, Y. L. Magnetic Weyl semimetal phase in a Kagomé crystal. *Science* **365**, 1282-1285, doi:10.1126/science.aav2873 (2019).
15 Yin, J.-X., Zhang, S. S., Chang, G., Wang, Q., Tsirkin, S. S., Guguchia, Z., Lian, B., Zhou, H., Jiang, K., Belopolski, I., Shumiya, N., Multer, D., Litskevich, M., Cochran, T. A., Lin, H., Wang, Z., Neupert, T., Jia, S., Lei, H. & Hasan, M. Z. Negative flat band magnetism in a spin–orbit-coupled correlated kagome magnet. *Nature Physics* **15**, 443-448, doi:10.1038/s41567-019-0426-7 (2019).

16 Tang, E., Mei, J.-W. & Wen, X.-G. High-Temperature Fractional Quantum Hall States. *Physical Review Letters* **106**, 236802, doi:10.1103/PhysRevLett.106.236802 (2011).
17 Neupert, T., Santos, L., Chamon, C. & Mudry, C. Fractional Quantum Hall States at Zero Magnetic Field. *Physical Review Letters* **106**, 236804, doi:10.1103/PhysRevLett.106.236804 (2011).
18 Xu, G., Lian, B. & Zhang, S.-C. Intrinsic Quantum Anomalous Hall Effect in the Kagome Lattice $Cs_2(LiMn)_3F_{12}$. *Physical Review Letters* **115**, 186802, doi:10.1103/PhysRevLett.115.186802 (2015).
19 Jiang, W., Kang, M., Huang, H., Xu, H., Low, T. & Liu, F. Topological band evolution between Lieb and kagome lattices. *Physical Review B* **99**, 125131, doi:10.1103/PhysRevB.99.125131 (2019).
20 Yin, J.-X., Ma, W., Cochran, T. A., Xu, X., Zhang, S. S., Tien, H.-J., Shumiya, N., Cheng, G., Jiang, K., Lian, B., Song, Z., Chang, G., Belopolski, I., Multer, D., Litskevich, M., Cheng, Z.-J., Yang, X. P., Swidler, B., Zhou, H., Lin, H., Neupert, T., Wang, Z., Yao, N., Chang, T.-R., Jia, S. & Zahid Hasan, M. Quantum-limit Chern topological magnetism in $TbMn_6Sn_6$. *Nature* **583**, 533-536, doi:10.1038/s41586-020-2482-7 (2020).
21 Asaba, T., Thomas, S. M., Curtis, M., Thompson, J. D., Bauer, E. D. & Ronning, F. Anomalous Hall effect in the kagome ferrimagnet $GdMn_6Sn_6$. *Physical Review B* **101**, 174415, doi:10.1103/PhysRevB.101.174415 (2020).
22 Ma, W., Xu, X., Yin, J. X., Zhou, H., Huang, Y., Hasan, M. Z. & Jia, S. Rare earth engineering in RMn_6Sn_6 topological kagome magnets. *https://arxiv.org/abs/2007.09913* (2020).
23 Wang, Q., Neubauer, K. J., Duan, C., Yin, Q., Fujitsu, S., Hosono, H., Ye, F., Zhang, R., Chi, S., Krycka, K., Lei, H. & Dai, P. Field-induced topological Hall effect and double-fan spin structure with a c-axis component in the metallic kagome antiferromagnetic compound YMn_6Sn_6. *Physical Review B* **103**, 014416, doi:10.1103/PhysRevB.103.014416 (2021).
24 Ghimire, N. J., Dally, R. L., Poudel, L., Jones, D. C., Michel, D., Magar, N. T., Bleuel, M., McGuire, M. A., Jiang, J. S., Mitchell, J. F., Lynn, J. W. & Mazin, I. I. Competing magnetic phases and fluctuation-driven scalar spin chirality in the kagome metal YMn_6Sn_6. *Science Advances* **6**, eabe2680, doi:10.1126/sciadv.abe2680 (2020).
25 Venturini, G., Fruchart, D. & Malaman, B. Incommensurate magnetic structures of RMn_6Sn_6 (R = Sc, Y, Lu) compounds from neutron diffraction study. *Journal of Alloys and Compounds* **236**, 102-110, doi:https://doi.org/10.1016/0925-8388(95)01998-7 (1996).
26 Rosenfeld, E. V. & Mushnikov, N. V. Double-flat-spiral magnetic structures: Theory and application to the RMn_6X_6 compounds. *Physica B: Condensed Matter* **403**, 1898-1906, doi:https://doi.org/10.1016/j.physb.2007.10.220 (2008).
27 Malaman, B., Venturini, G., Welter, R., Sanchez, J. P., Vulliet, P. & Ressouche, E. Magnetic properties of RMn_6Sn_6 (R=Gd–Er) compounds from neutron diffraction and Mössbauer measurements. *Journal of Magnetism and Magnetic Materials* **202**, 519-534, doi:https://doi.org/10.1016/S0304-8853(99)00300-5 (1999).
28 Venturini, G. Antiferro- to ferromagnetic transition in $HfFe_6Ge_6$-type solid solution $YMn_6Ge_{6-x}Ga_x$ ($0.25 \leqslant x \leqslant 2.00$). *Journal of Alloys and Compounds* **311**, 101-108, doi:https://doi.org/10.1016/S0925-8388(00)00816-1 (2000).
29 Venturini, G., Vernière, A. & Malaman, B. A neutron diffraction study of $HfFe_6Ge_6$-type $LuMn_6Ge_{6-x}Ga_x$ compounds (x=0.4, 0.7 and 1.0). *Journal of Alloys and Compounds* **319**, 22-28, doi:https://doi.org/10.1016/S0925-8388(01)00882-9 (2001).
30 Mazet, T., Venturini, G., Welter, R. & Malaman, B. A magnetic study of $Mg_{1-x}Ca_xMn_6Sn_6$ compounds ($0.0 \leqslant x \leqslant 0.7$).: First example of ferromagnetic $HfFe_6Ge_6$-type structure compounds. *Journal of Alloys and Compounds* **264**, 71-75, doi:https://doi.org/10.1016/S0925-8388(97)00265-X (1998).

31 Matsuo, A., Suga, K., Kindo, K., Zhang, L., Brück, E., Buschow, K. H. J., Boer, F. R. d., Lefèvre, C. & Venturini, G. Study of the Mn–Mn exchange interactions in single crystals of RMn_6Sn_6 compounds with R=Sc, Y and Lu. *Journal of Alloys and Compounds* **408-412**, 110-113, doi:https://doi.org/10.1016/j.jallcom.2005.04.080 (2006).

32 See the Supplementla Materials.

33 Zhang, S.-y., Zhao, P., Cheng, Z.-h., Li, R.-w., Sun, J.-r., Zhang, H.-w. & Shen, B.-g. Magnetism and giant magnetoresistance of $YMn_6Sn_{6-x}Ga_x$ (x=0--1.8) compounds. *Physical Review B* **64**, 212404, doi:10.1103/PhysRevB.64.212404 (2001).

34 Zhang, H., Feng, X., Heitmann, T., Kolesnikov, A. I., Stone, M. B., Lu, Y. M. & Ke, X. Topological magnon bands in a room-temperature kagome magnet. *Physical Review B* **101**, 100405, doi:10.1103/PhysRevB.101.100405 (2020).

35 Li, M., Wang, Q., Wang, G., Yuan, Z., Song, W., Lou, R., Liu, Z. K., Huang, Y., Liu, Z., Lei, H., Yin, Z. & Wang, S. Spin-polarized Dirac cone, flat band and saddle point in kagome magnet YMn_6Sn_6. *https://assets.researchsquare.com/files/rs-114140/v1_stamped.pdf* (2020).